



Input-Output Analysis of Shock Boundary Layer Interaction

Anubhav Dwivedi^{*}, Sidharth GS[†], Graham V. Candler[‡], and Joseph W. Nichols[§]
University of Minnesota, Minneapolis, MN, 55455

Mihailo R. Jovanović[¶]
University of Southern California, Los Angeles, CA, 90089-2560

Understanding transition mechanisms in high speed boundary layers is important for predictive design and control in aeronautics. Shock boundary layer interaction, in which the inviscid pressure rise causes the incoming boundary layer to separate and reattach downstream, has a destabilizing effect on the flow. The presence of a recirculation bubble and highly concave curvature of the streamlines near reattachment can support large growth of perturbations. In this paper, we investigate the receptivity properties of an asymptotically stable shock boundary layer interaction on a slender double wedge. The optimal frequency response of the two-dimensional steady state flow subjected to external perturbations is computed. It is found that the flow is highly receptive to low-frequency streamwise vorticity perturbations of a specific spanwise wavelength in the incoming boundary layer. This results in growth of streaks post-reattachment. The most amplified spanwise wavelength scales with approximately twice the boundary layer thickness at reattachment. By excluding the role of bubble dynamics in the input-output analysis, we find that recirculation bubble plays an important role in the perturbation growth and the spanwise wavelength selection. The present work demonstrates the efficacy of input-output analysis for investigating the stability and sensitivity of compressible boundary layer flows.

I. Introduction

High speed flow over a double-wedge is a canonical case of shock boundary layer interaction [1]. Flow deflection at the compression corner can cause the laminar boundary layer to separate due to the inviscid pressure rise. This is associated with a separation/reattachment shock system. Experiments on supersonic and hypersonic flow on compression ramps and double wedges exhibit three-dimensionality in the form of streamwise striations or streaks in wall temperature near reattachment, that persist downstream. Streamwise vortical structures associated with these streaks result in heat transfer with large local peaks in span. The three-dimensional flow structures have a destabilizing effect on the boundary layer and play a role in the transition process [2, 3].

Streamwise streaks are observed in compression corner experiments over a range of Mach numbers, turn angles and wall temperatures [4–7]. The presence of streaks near reattachment is not restricted to compression ramps[2]. For example, they also appear in axisymmetric geometries such as the hollow cylinder-flare [8] and oblique shock boundary layer interaction [9]. The wavelength associated with the streamwise streaks is usually on the order of twice the boundary layer thickness at reattachment [4, 10]. De Luca *et al.* [11] and De la Chevalerie *et al.* [12] studied the role of the unit Reynolds number and the leading-edge to corner distance on the spanwise wavelength of the streaks on a Mach 7 15° compression ramp. The wavelength was found to decrease with increasing unit Reynolds number and with decreasing flat plate length. This suggests that the wavelength of the streamwise vortices is affected by the local boundary layer thickness.

The observed streaks are often attributed to Görtler-like vortices [13] that arise from destabilizing centrifugal forces near reattachment where the streamline curvature is highly concave. Görtler instability implies a role of upstream perturbations [14] in the formation of streaks. Therefore, some studies have proposed leading edge imperfections as the origin of streamwise streaks. Chuvakhov *et al.* [15] and Roghelia *et al.* [4] showed that increasing leading edge bluntness alters the spanwise heat flux pattern on Mach 8 flow over compression ramps.

^{*}Graduate Research Assistant, Aerospace Engineering and Mechanics, AIAA Student Member

[†]Graduate Research Assistant, Aerospace Engineering and Mechanics, AIAA Student Member

[‡]Russell J. Penrose and McKnight Presidential Professor, Aerospace Engineering and Mechanics, AIAA Fellow

[§]Assistant Professor, Aerospace Engineering and Mechanics

[¶]Professor, Ming Hsieh Department of Electrical Engineering, APS fellow

Computational studies investigating the development of streamwise streaks have been performed by Yao et al. [16] and Navarro-Martinez and Tutty [17]. Yao et al. [16] consider development of perturbations in transitional interaction at Mach 4.5 induced by upstream stochastic forcing. Streamwise elongated structures are seen to dominate the flow dynamics leading to transition. Navarro and Tutty [17] used steady in time spanwise periodic upstream forcing on a three dimensional ramp at Mach 6.85. They found that forcing near the leading edge produced higher amplification than forcing close to the separation point.

Recent studies have focused on global three-dimensional instabilities in shock boundary layer interaction and their role in formation of streaks downstream. This approach investigates the intrinsic stability of the linearized system in absence of any external perturbations. Robinet[18] and Hildebrand et al.[19] have applied global stability analysis to study the bifurcation of the nominally two-dimensional interaction to three dimensionality in Mach 2.15 and Mach 5.92 oblique shock interactions, respectively. More recently, GS *et al.* [20] reported a similar three-dimensional global instability on a slender double wedge and found that the instability can result in temperature streaks post-reattachment..It is interesting to note that the global instability in both these interactions [19, 20] does not appear to have a centrifugal origin. Also, the spanwise length scale of the instability scales with the separation bubble length rather than the incoming or reattaching boundary layer thickness.

In addition to bifurcation in flow state due to emergence of instability, numerous works [21, 22] have pointed out the important role played by the non-normality of the linearized Navier-Stokes operator [22–24] in perturbation amplification. However, most of the previous work has focused on transient amplification of initial conditions [25–28]. In this work, we adopt a different perspective, in which amplification properties of the forced linear compressible Navier Stokes equations are considered with initial conditions set to zero. This idea has been applied to investigate the receptivity of hypersonic boundary layers [29–31] . However, instead of investigating the receptivity to free-stream or upstream excitations, we consider receptivity of flow field to the spatio-temporal distribution of mass, momentum and internal energy perturbations.

The input-output analysis of linear systems is a common approach in systems theory [32, 33]. This approach has been used to study subcritical transition in canonical incompressible flow configurations [24, 34]. Recently, Brandt *et al.* [35] used a similar approach to investigate the effect of Reynolds number and leading edge radius on incompressible boundary layers. For compressible flows, recent work by Jeun et al. [36] considered this approach for far-field acoustic amplification from a turbulent jet using the compressible Euler equations. Pando and Schmid [37] applied this approach in subsonic compressible flow over isolated roughness elements. All of these applications help establish that frequency-response analysis is effective when multiple physical processes compete in establishing observed amplification mechanisms. A judicious choice for input and output weights can help explore and quantify a multitude of energy amplification mechanisms through a network of possible interactions.

In the current work we apply input-output (I/O) analysis to high-speed compressible boundary layers. First, we investigate the relevance of this approach in a canonical flow configuration of flow over a flat plate. Next, we use this approach to understand the I/O behavior of shock boundary layer interaction (SBLI) in high speed flow over a slender double wedge. We investigate the role of SBLI by first evaluating optimal frequency response of the flow over a slender wedge with no turn angle. Later, we introduce a turn angle and then quantify the role played by recirculation bubble and the streamwise curvature in the emergence of streaks by external perturbations.

II. Methodology for linear analysis

A. Linearized compressible flow equations

The compressible Navier-Stokes equations in the conservative form can be written as

$$\frac{\partial \mathbf{U}}{\partial t} + \frac{\partial \mathbf{F}_j}{\partial x_j} + \frac{\partial \mathbf{F}_j^v}{\partial x_j} = 0 \quad (1)$$

where \mathbf{U} is the vector of conserved solution variables, \mathbf{F}_j is the inviscid flux vector and \mathbf{F}_j^v is the viscous flux vector.

$$\mathbf{U} = \begin{pmatrix} \rho \\ \rho u_i \\ E \end{pmatrix}, \mathbf{F}_j = \begin{pmatrix} \rho u_j \\ \rho u_i u_j + p \delta_{ij} \\ (E + p)u_j \end{pmatrix}, \mathbf{F}_j^v = \begin{pmatrix} 0 \\ \sigma_{ij} \\ \sigma_{ij} u_i + q_j \end{pmatrix} \quad (2)$$

The viscous momentum flux is $\sigma_{ij} = -\mu(S_{ij} - 2/3 S_{kk} \delta_{ij})$ and the molecular heat diffusion is $q_j = -\kappa \partial_j T$. Conductivity κ for air is evaluated corresponding to a Prandtl number $Pr \approx 0.72$. To analyze the behavior of small fluctuations about the base flows, the compressible Navier-Stokes equations Eq. 1 are linearized. The conserved flow variables are decomposed into the base and small fluctuation components, $\bar{\mathbf{U}} + \mathbf{U}'$. The superscript "'' denotes the perturbation quantities and the overbar denotes the base flow variables. The convective flux can be expanded using Taylor series about $\bar{\mathbf{U}}$ as,

$$\mathbf{F}_j(\mathbf{U}) = \mathbf{F}_j(\bar{\mathbf{U}}) + \left. \frac{\partial \mathbf{F}_j}{\partial \mathbf{U}} \right|_{\bar{\mathbf{U}}} \mathbf{U}' + \mathbf{O}(\mathbf{U}'^2) \quad (3)$$

The viscous flux involves spatial gradients in the primitive variable set, $\mathbf{V}^T = (\rho, u, v, w, T)$ and can be written in the form[38],

$$\mathbf{F}_j^v = \mathbf{M}_{jk} \frac{\partial}{\partial x_k} \mathbf{V} \quad (4)$$

and decomposed into the base state viscous flux and perturbation flux as,

$$\mathbf{F}_j^v(\mathbf{U}) = \mathbf{F}_j^v(\bar{\mathbf{U}}) + \bar{\mathbf{M}}_{jk} \frac{\partial}{\partial x_k} \mathbf{V}' + \bar{\mathbf{M}}_j^{\text{VD}} \mathbf{V}' \quad (5)$$

The matrices \mathbf{M}_{ij} contain the transport coefficients, and can be found in the Appendix. We do not consider terms that arise from perturbations in viscosity μ' due to perturbations in temperature. The term $\bar{\mathbf{M}}_j^{\text{VD}}$ is a rank 1 tensor and arises from linearization of the viscous dissipation $\sigma_{ij} u_i$ term. Subtracting the governing equations for the base flow state $\bar{\mathbf{U}}$ from Eq. 1, we obtain the governing equations for small compressible perturbation,

$$\begin{aligned} \frac{\partial \mathbf{U}'}{\partial t} + \frac{\partial}{\partial x_j} (\bar{\mathbf{A}}_j + \bar{\mathbf{A}}_j^v) \mathbf{U}' &= 0 \\ \bar{\mathbf{A}}_j &= \frac{\partial \bar{\mathbf{F}}_j}{\partial \bar{\mathbf{U}}}, \quad \bar{\mathbf{A}}_j^v = \left(\bar{\mathbf{M}}_{jk} \frac{\partial}{\partial x_k} + \bar{\mathbf{M}}_j^{\text{VD}} \right) \bar{\mathbf{N}} \end{aligned} \quad (6)$$

Since perturbations are small, the conserved variable set \mathbf{U}' and the primitive variable set \mathbf{V}' can be linearly transformed. Here, the matrix $\bar{\mathbf{N}}$ is the transformation matrix such that $\mathbf{V}' = \bar{\mathbf{N}} \mathbf{U}'$. The value of $\bar{\mathbf{N}}$ can be found in the appendix. The use of conserved perturbation variables results in a conserved form of linear governing equations. For simplicity of further analysis, we represent Eq. 6 in the following form,

$$\frac{\partial}{\partial t} \mathbf{q}(\mathbf{x}, t) = \mathcal{A}(\mathbf{x}) \mathbf{q}(\mathbf{x}, t) \quad (7)$$

Here, $\mathbf{q}(\mathbf{x}, t) = \mathbf{U}'$ represents the fluctuation state at each point in the domain and $\mathcal{A}(\mathbf{x})$ represents the linear compressible Navier Stokes equations as linear time invariant system [21, 32, 34].

B. Frequency response and input-output analysis

The previous section described the linearized compressible Navier Stokes equations about a steady base state. To analyze the input-output behavior of the linearized dynamics, we represent the forced compressible in state space form,

$$\begin{aligned} \frac{\partial}{\partial t} \mathbf{q}(\mathbf{x}, t) &= \mathcal{A}(\mathbf{x}) \mathbf{q}(\mathbf{x}, t) + \mathcal{B}(\mathbf{x}) \mathbf{d}(\mathbf{x}, t) \\ \phi(\mathbf{x}, t) &= \mathcal{C}(\mathbf{x}) \mathbf{q}(\mathbf{x}, t) \end{aligned} \quad (8)$$

As mentioned previously, $\mathbf{q}(\mathbf{x}, t) = \mathbf{U}' = [\rho' \ (\rho u)' \ (\rho v)' \ (\rho w)' \ (E)']^T$ represents the state of the linear system, $\phi(\mathbf{x}, t)$ represents the measured or 'output' variables and $\mathbf{d}(\mathbf{x}, t)$ spatially distributed and temporally varying perturbation source term. In general, these operators, $\mathcal{A}(\mathbf{x})$, $\mathcal{B}(\mathbf{x})$ and $\mathcal{C}(\mathbf{x})$ can be used to describe linear evolution of fluctuations to any external 'inputs' or excitations, $\mathbf{d}(\mathbf{x}, t)$. The form of $\mathcal{B}(\mathbf{x})$ and $\mathcal{C}(\mathbf{x})$ used in this work is shown in the appendix.

In the current work, we assume that the base flow quantities do not vary along the span (along z -axis). This allows us to take a Fourier transform in the spanwise direction. Furthermore, we assume the input \mathbf{d} is harmonic in time which makes the input field $\mathbf{d}(\mathbf{x}, t)$ take the following form,

$$\mathbf{d}(\mathbf{x}, t) = \mathbf{d}(x, y) e^{i(\beta z + \omega t)} \quad (9)$$

This allows us (after assumptions on stability of \mathcal{A}) to write the following input-output relationship,

$$\phi(x, y, \beta, \omega) = [\mathcal{H}\mathbf{d}](x, y, \beta, \omega) \quad (10)$$

where, the operator $\mathcal{H}(x, y, \beta, \omega)$ is given by

$$\mathcal{H}(x, y, \beta, \omega) = \mathcal{C}(x, y, \beta, \omega)(i\omega\mathbf{I} - \mathcal{A}(x, y, \beta, \omega))^{-1} \mathcal{B}(x, y, \beta, \omega) \quad (11)$$

Next, we quantify the ‘gain’ or the ‘amplification’ of the system given by Eq. 10 as follows,

$$G^2(\omega, \beta) := \max_{\mathbf{d}} \frac{\|\phi\|_E}{\|\mathbf{d}\|_E} \quad (12)$$

This defines the optimal frequency response as the ratio of the energy-based output norm to the energy-based input norm, optimized over all possible inputs \mathbf{d} . The specific energy to measure the disturbance size is Chu’s energy measure for compressible flows [28, 39]. This leads to the following definition of the scalar inner product and the disturbance energy norm,

$$\langle \psi_1, \psi_2 \rangle_E = \langle \psi_1, \mathbf{P}\psi_2 \rangle \quad \|\psi\|_E^2 = \langle \psi, \psi \rangle_{\mathbf{P}} \quad (13)$$

Here, \mathbf{P} is a symmetric positive definite matrix. The definition of \mathbf{P} for the conserved perturbation quantities is given in the Appendix.

C. Numerical discretization and optimization problem

In the present study, for the computation of all the base flow we use US3D [40], an unstructured finite volume solver. For the discretization of the linear system Eq. 6 we use a second order central finite volume scheme. More details about the discretization and its implementation can be found in recent work by GS *et al.* [20, 41].

After discretization we can rewrite the gain (Eq. 12) from the input-output analysis as,

$$G_D^2(\omega, \beta) := \max_{\mathbf{d}_D} \frac{\phi_D^H \mathbf{P}_D \phi_D}{\mathbf{d}_D^H \mathbf{P}_D \mathbf{d}_D} \quad (14)$$

Here, the terms with subscript \mathbf{D} denote the discretized vectors in the computational domain and \mathbf{H} denotes Hermitian transpose. The matrix \mathbf{P}_D is the discrete version of the operator \mathbf{P} given in Eq. 13. It is positive definite as well but now also contains the grid metric for the computational domain. However, from this point we will drop these subscript for the ease of notation.

We can rewrite the problem of finding the maximum gain (Eq. 14) in the following form,

$$\begin{aligned} \min_{\mathbf{d}} \quad & \frac{\mathbf{d}^H \mathbf{P} \mathbf{d}}{(\mathbf{C}\mathbf{q})^H \mathbf{P} (\mathbf{C}\mathbf{q})} \\ \text{subject to} \quad & (i\omega\mathbf{I} - \mathbf{A})\mathbf{q} = \mathbf{B}\mathbf{d} \end{aligned} \quad (15)$$

Here, the operators, \mathbf{A} , \mathbf{B} and \mathbf{C} are the discretized version of the operators \mathcal{A} , \mathcal{B} and \mathcal{C} used in Eq. 8. The matrix \mathbf{A} includes the boundary conditions on perturbation quantities. We assume Dirichlet boundary condition on velocity and Neumann boundary condition on pressure and density. This is a constrained optimization problem involving a quadratic form. The solution to this can be easily obtained by computing the singular value decomposition (SVD). Where,

$$\mathbf{P}^{1/2} \bar{\mathbf{H}} \mathbf{P}^{-1/2} = \mathbf{U} \Sigma \mathbf{V}^H \quad (16)$$

Here, $\bar{\mathbf{H}}$ is the discretized version of $\mathcal{H}(x, y, \beta, \omega)$ in Eq. 11. Using Eq. 16 we can characterize the optimal frequency response behavior of a given base state as follows,

$$\begin{aligned} \text{Optimal input:} \quad & \mathbf{d}_{\text{opt}} = \mathbb{P}^{-1/2} \mathbf{v}_1 \\ \text{Optimal response:} \quad & \phi_{\text{opt}} = \mathbb{P}^{-1/2} \mathbf{u}_1 \\ \text{Optimal amplification:} \quad & G = \sigma_1 \end{aligned} \tag{17}$$

Here, \mathbf{u}_1 and \mathbf{v}_1 column vectors of \mathbf{U} and \mathbf{V} and σ_1 is the maximum singular value. In the present work, we use an iterative algorithm to compute the optimal gain and input and response vectors. Details of the algorithm can be found in the Appendix. It is important to point out that by systematic construction of the input matrix \mathbf{B} and response matrix \mathbf{C} can be used to restrict the input entering the system and the observed output [36, 37].

III. Results

We use the ‘input-output’ (I/O) approach to evaluate optimal frequency response of high speed compressible boundary layers. First, we analyze a canonical configuration of the flow over a flat plate and illustrate the usefulness of this approach in quantifying frequency response of flow field. Then we apply this methodology to high speed flow over a slender double wedge considered in previous work [20, 41] to investigate formation of streaks in shock boundary layer interactions (SBLI).

A. I/O analysis of flow over a flat plate

The flow over an adiabatic flat plate with sharp leading edge at Mach 4.5 is considered. Previous work on the receptivity of disturbances under these flow conditions was reported by Ma and Zhong [30]. The objective of this section is to use this well studied flow configuration to verify that the results from the I/O analysis approach canonical behavior under appropriate constraints on input and output locations.

The flow configuration and the description of the free stream condition is shown schematically in Fig. 1. For analyzing boundary layer instability, a local Reynolds number, R based on the viscous length scale associated with the boundary layer thickness is used. This is defined as,

$$R = \sqrt{Re_x} = \frac{\rho_{\infty}^* U_{\infty}^* l^*}{\mu_{\infty}^*}, \quad l^* = \sqrt{\frac{\mu_{\infty}^* x^*}{\rho_{\infty}^* U_{\infty}^*}} \tag{18}$$

Further, non-dimensional frequency is,

$$F = \frac{\omega^* \mu_{\infty}^*}{\rho_{\infty}^* U_{\infty}^{*2}} \tag{19}$$

All the starred quantities denote dimensional variables and all the quantities with subscript ∞ denote freestream variables. In this work, we consider a plate with a length of 0.4m. In terms of the local Reynolds number, the domain spans from $R = 0$ to $R = 1697$. Two non-dimensional frequencies are considered, $F = 1.6 \times 10^{-4}$ and 2.2×10^{-4} .

Ma and Zhong [30] report that for $F = 2.1 \times 10^{-4}$ the base flow is unstable in the region between $R \approx 840$ to 1030 (i.e. $x^* \approx 0.09\text{m}$ to 0.145m) from LST (linear stability theory)[42], while for $F = 1.6 \times 10^{-4}$ the base flow is unstable from $R \approx 1155$ to 1416.3 (i.e. $x^* \approx 0.185\text{m}$ to 0.27m). Physically, these locations correspond to regions in space where, for a given temporal frequency, spatial growth of a wavepacket occurs due to local linear instability. Next, we use the I/O analysis to check if it can produce similar spatial characteristics.

As mentioned earlier, the use of matrices \mathbf{B} and \mathbf{C} (Eq. 15) can be used to restrict the input region and the observed response, respectively. For this flow field, we modify \mathbf{B} to restrict the input at $R = 388.8$ (i.e. $x^* \approx 0.021\text{m}$) for both the frequencies (see Fig. 1 for a schematic). However, response in the entire domain is evaluated. To model the finite extent of the domain, perturbations are made to decay in the free stream and at inflow and the outflow boundaries using numerical sponge zones. The optimization problem described in Eq. 15 is solved individually for both frequencies considered. The inputs and the outputs are considered to be two dimensional and hence the spanwise wavenumber, β is set to zero in both cases. The algorithm converges in 4 – 5 iterations for all the computations. The spatial response obtained for both frequencies is shown in Fig. 2

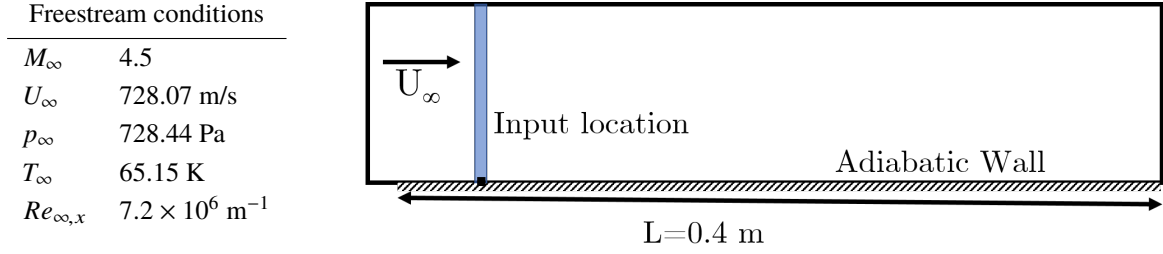


Fig. 1 Free-stream conditions, schematic of the geometry. The flow conditions are taken from Ma and Zhong [30]. We assume an adiabatic wall for the base flow computations. For I/O analysis, the input location is shown schematically with the blue band

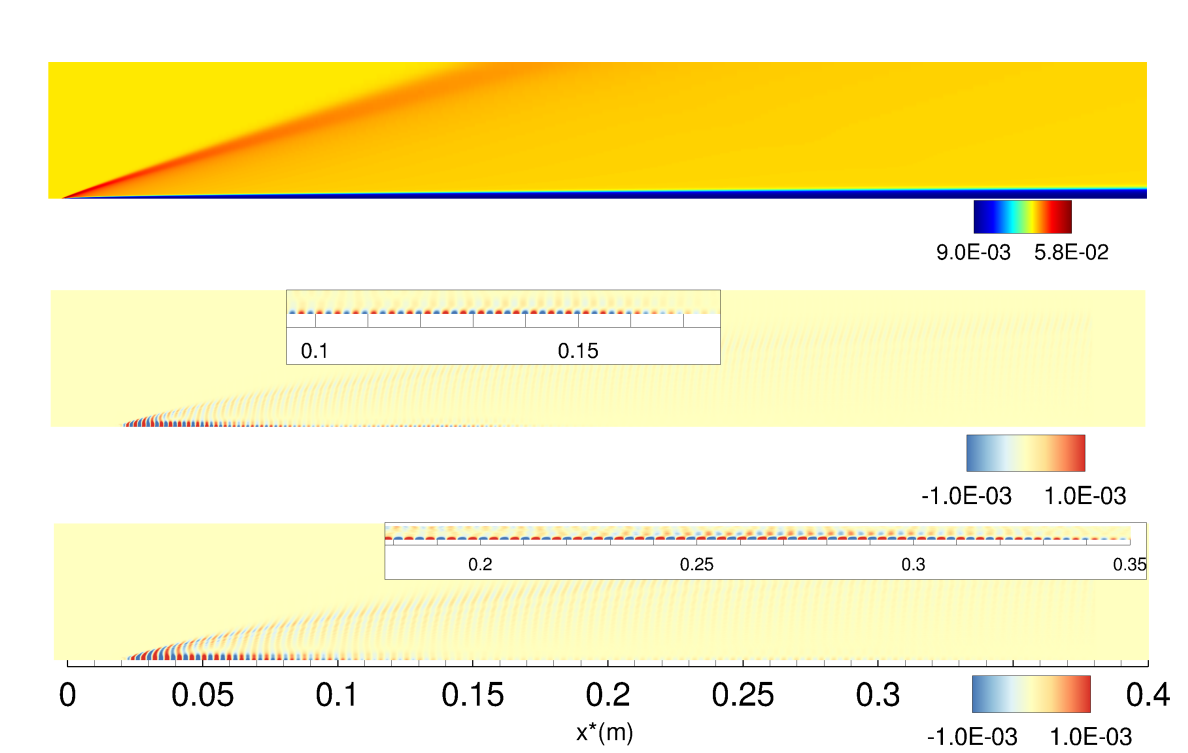


Fig. 2 The optimal response of flow over a flat plate with sharp leading edge. (a) The base density profile. (b) and (c) show optimal response using pressure perturbation for $F = 2.2 \times 10^{-4}$ and $F = 1.6 \times 10^{-4}$ respectively. Insets in (b) and (c) also show zoomed in view of the perturbation growth due to local spatial instability.

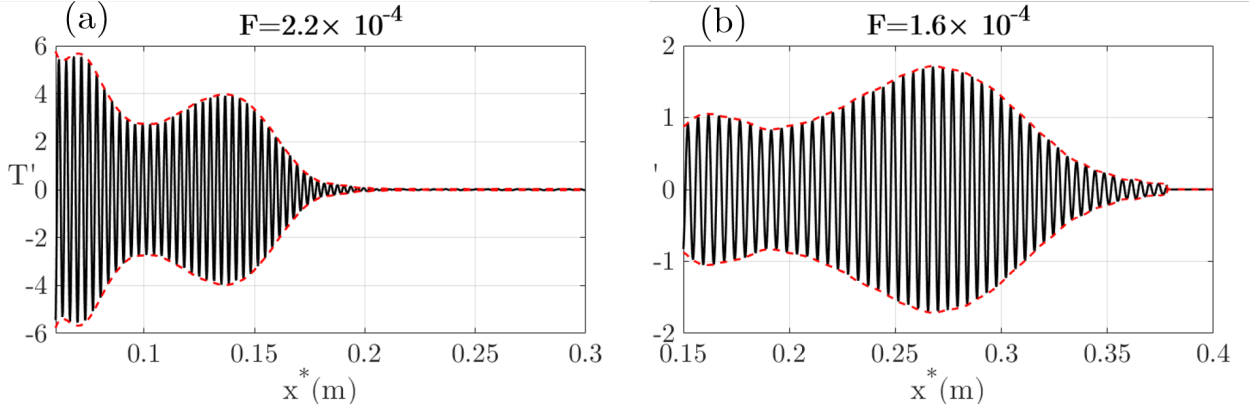


Fig. 3 Temperature perturbation of the optimal response close to the wall with distance x^* . Here, (a) denotes the spatial growth for $F = 2.2 \times 10^{-4}$ and $F = 1.6 \times 10^{-4}$ respectively.

From Fig. 2, we see that there is large growth in space downstream near the location of the input at $x^* = 0.021$. This large growth in space can be attributed to the Orr mechanism [43], involving transient spatial growth due to perturbations which tilt away from the mean shear. For both frequencies, this growth appears and decays quickly downstream. Further downstream perturbations start amplifying in the regions of local modal spatial instability. This downstream amplification is clearly shown in Fig. 3 where streamwise variation of the temperature perturbation response near the wall is plotted for both frequencies. For $F = 2.2 \times 10^{-4}$ we observe local amplification starting from $R = 805$ to $R = 1014$ (i.e. $x^* = 0.09$ to 0.143) and no further amplification is then observed anywhere in space. For $F = 1.6 \times 10^{-4}$ we observe local amplification starting from $R = 1138.4$ to $R = 1407.2$ (i.e. $x^* = 0.18$ to 0.275).

We also compute the local spatial growth rate from the optimal response at both these frequencies. To do this, we first assume that the amplitude and phase of response can be decomposed as $\phi'(x, y, \omega) = |\phi'(x, y)|e^{i\psi'(x)}$ at a given ω . We can then evaluate the growth rate using the following equation,

$$\alpha_i = -\frac{1}{|\phi'|} \frac{d|\phi'|}{dx} \quad (20)$$

Fig. 4 shows the variation of local spatial growth rate computed using Eq. 20 with non-dimensional circular frequency. The growth rate predictions for both cases are close to those predicted by LST. Further, I/O analysis correctly identifies the regions in space where the second mode becomes unstable. However, there are some differences that can be attributed to non-parallel behavior of the boundary layer which is neglected in LST. Some of the differences in the curves can be attributed to differences in the base flow between this study and that computed by Ma and Zhong [30].

From this analysis, we conclude that by computing the frequency response within the framework of I/O analysis, we can investigate the spatio-temporal amplification properties without making any simplifications to the linearized governing equations. In particular, both modal and non-modal behavior can be captured which cannot be captured using methodology like LST or PSE [44], which make *a priori* assumptions on the form of the perturbations. Further, by using different **B** and **C** (in Eq. 14) we can explore and isolate various paths of energy amplification in any given flow field.

B. I/O analysis of high speed flow over a slender double wedge

High speed flow over a slender double wedge is a canonical geometry for shock boundary layer interaction. The rapid rise in pressure leads to flow separation and formation of a separation bubble. Many experimental studies [3, 4, 15, 45] report steady and regular short-wavelength spanwise heat transfer striations near boundary layer reattachment. These striations are attributed to the formation of Görtler-type vortices due to the concave flow curvature near the reattachment. These patterns are not related to finite span effects [3]. It is postulated that the free stream noise in wind tunnels as well as imperfections in leading edges can introduce perturbations which can be amplified by the bubble and the streamline curvature near the reattaching shear layer [45, 46]. However, a detailed understanding of how these uncertainties (imperfections in leading edge, etc.) manifest in the flow field and are ‘amplified’ to produce three dimensional flow structures is lacking. The present work aims to answer this question.

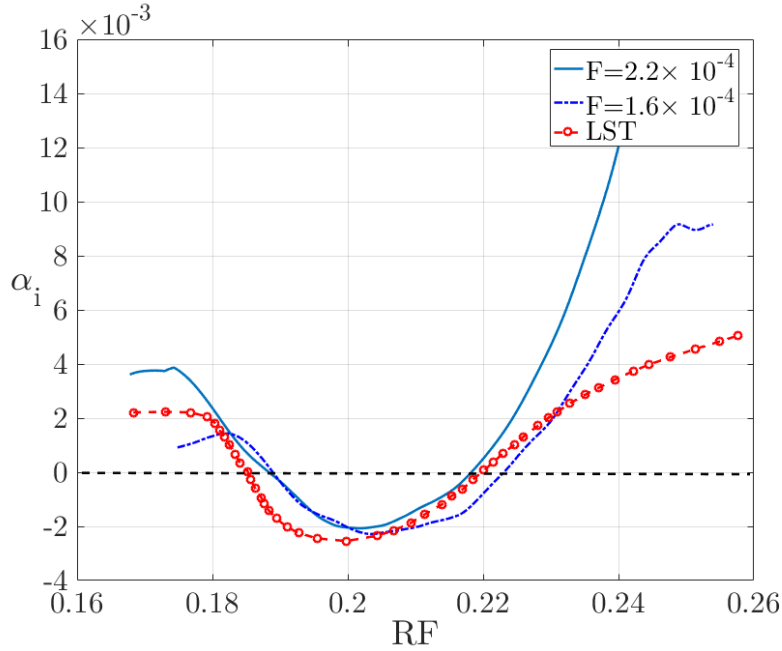


Fig. 4 Comparison of spatial growth rate versus non-dimensional circular frequency, $\omega = RF$ predicted using LST (reproduced from Ma and Zhong [30]) and observed from I/O optimal response.

The free stream condition in this work correspond to the experiment conducted in the High SuperSonic Tunnel (HSST) of the University of Manchester [47]. The free stream flow conditions and the schematic of the $12^\circ/19.5^\circ$ double wedge geometry is shown in Fig. 5. The turn angle is $\theta = 7.5^\circ$. We will investigate the frequency response of two-dimensional steady state flow past the double wedge configuration within the framework of I/O analysis.

The 2D steady state solution computed by the flow solver [40] is shown in Fig. 6. We assume an adiabatic wall and perfect gas for obtaining the steady solution [20, 47]. The base flow is computed on a grid with 105K cells. Further details on the grid convergence can be found in the work by GS *et al.* [20, 41]. The boundary layer thickness (δ_{99}) at the reattachment location is 8×10^{-4} m. We will use this value to non-dimensionalize all the length scales. The corresponding time scale is defined as δ_{99}/U_∞ .

In the previous work [20, 41], the authors investigated the global stability characteristics of this flow field. The flow was found to be globally linearly stable for all the spanwise wavenumbers, β (where, $\beta = 2\pi/\lambda_z$). Before investigating the frequency response of this complex flow field, we consider a simpler flow field on a 12° wedge. The boundary layer is attached and there is no SBLI.

1. Frequency response of Mach 5 flow over a 12° wedge

The free-stream conditions as described in Fig. 5. Adiabatic wall and perfect gas assumed for computation of steady base flow. The computational domain comprises of 107K cells. The schematic of the flow configuration along with contours of density in the two dimensional flow field is shown in Fig. 7.

The 2D boundary layer over the wedge is globally stable [43]. Thus, the discretized matrix \mathbf{A} in Eq. 14 is stable and we can use the framework of I/O analysis to evaluate the frequency response of this flow field. For quantifying the worst case scenario, we allow the inputs on the entire domain and observe the response over the entire domain. This means that the discrete matrices \mathbf{B} and \mathbf{C} are identity. To model finite extent of the domain, perturbations are made to decay in the free stream and at the inflow and the outflow boundaries using numerical sponge zones. At the wall we assume Dirichlet boundary conditions on velocity perturbation and Neumann on pressure and density perturbations.

The maximum amplification or gain of the system's frequency response is parametrized in terms of the spanwise wavenumber, β and the circular frequency, ω and is shown in Fig. 8. The maximum amplification is observed for $\beta = 2.61$ and $\omega = 0.4$. This maximum in the frequency domain corresponds to oblique first mode. Steady perturbations show significantly lower amplification (shown in Fig. 8). The optimal response is shown in Fig. 9

Freestream conditions	
M_∞	5.0
U_∞	792.35 m/s
p_∞	1.22 kPa
T_∞	62.5 K
$Re_{\infty,x}$	$13.6 \times 10^6 \text{ m}^{-1}$

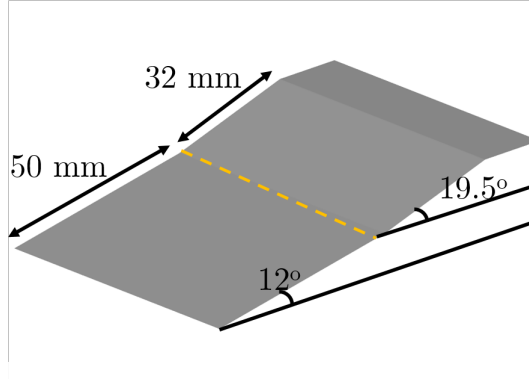


Fig. 5 Free-stream conditions, schematic of geometry of the flow over a slender double wedge at an angle of 12° . The flow turns through an angle of 7.5° . The flow conditions are taken from Yang *et al.* [47].

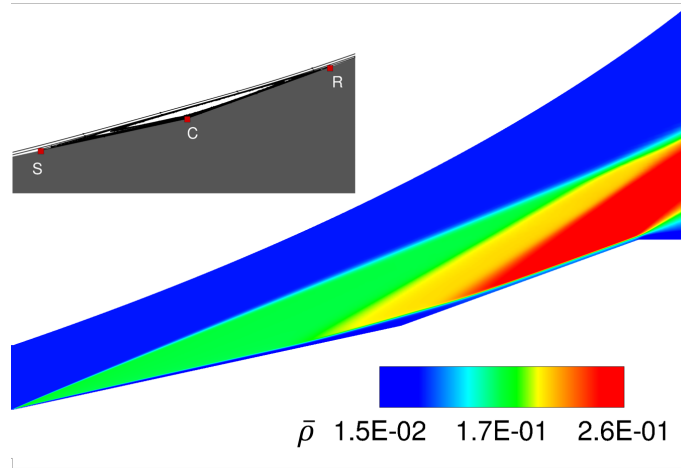


Fig. 6 Contours of density of the computed 2D base flow. Overset image on top left shows the separation bubble using streamlines. Separation (S), reattachment (R) and the corner point (C) are also marked

2. Frequency response of flow over a $12^\circ/19.5^\circ$ double wedge

Analysis of the 12° wedge in the previous section shows that for an attached boundary layer, maximum amplification occurs in the form of traveling oblique waves. Now, we consider the double wedge described in Fig. 5. As in the previous case, we allow the inputs on the entire domain and observe the response over the entire domain as well. Maximum gain as function of parameters ω and β is shown in Fig. 10(a). The gain associated with steady response, i.e. $\omega = 0$ is shown in Fig. 10(b).

We note that unlike the flow with no SBLI (see Fig. 8), largest amplification is observed for low frequencies (i.e. as $\omega \rightarrow 0$). Further, significant amplification occurs in a finite band of spanwise length scales ($\beta_{\max} \sim 0.6$, $\lambda_z \sim 2\delta_{99}$ at reattachment). In order to qualitatively understand the effect of SBLI, we compare frequency response at $\omega = 0$ for different spanwise wavenumber, β for turn angles 0° and 7.5° (single and double wedge respectively) in Fig. 10(b). The maximum growth is significantly larger in the presence of the bubble. We also note that as the spanwise wavenumber of the inputs decreases and becomes the same order as the length of the separation bubble ($\sim 10\delta$), the growth in both the cases starts to converge. This is expected, as the bubble is no longer relevant to the growth of the perturbations at extremely large spanwise length scales.

The spatial distribution of the input field resulting in this response is shown in Fig. 11(a). From this we see that the input consists of spanwise periodic, streamwise vortices in the incoming boundary layer as well as the separation bubble.

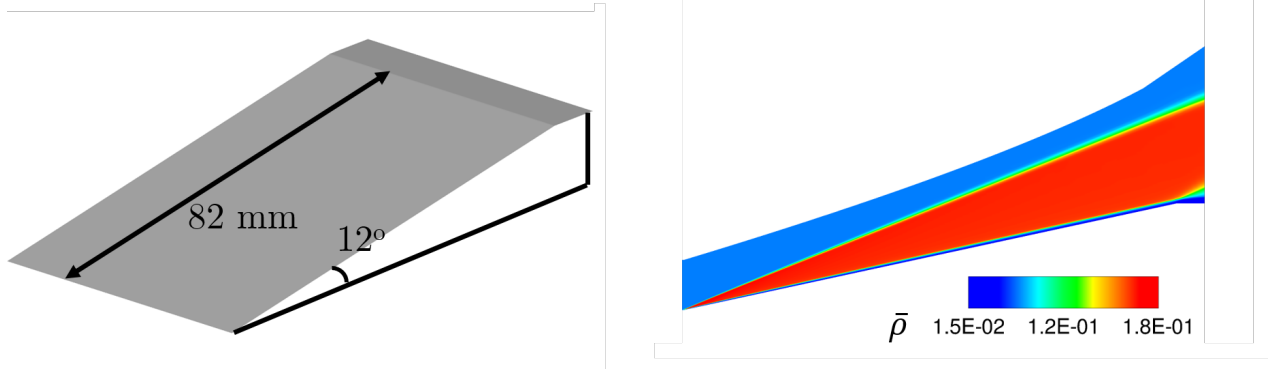


Fig. 7 Geometry for the flow over a 12° wedge (left); Density contours of the steady base flow (right)

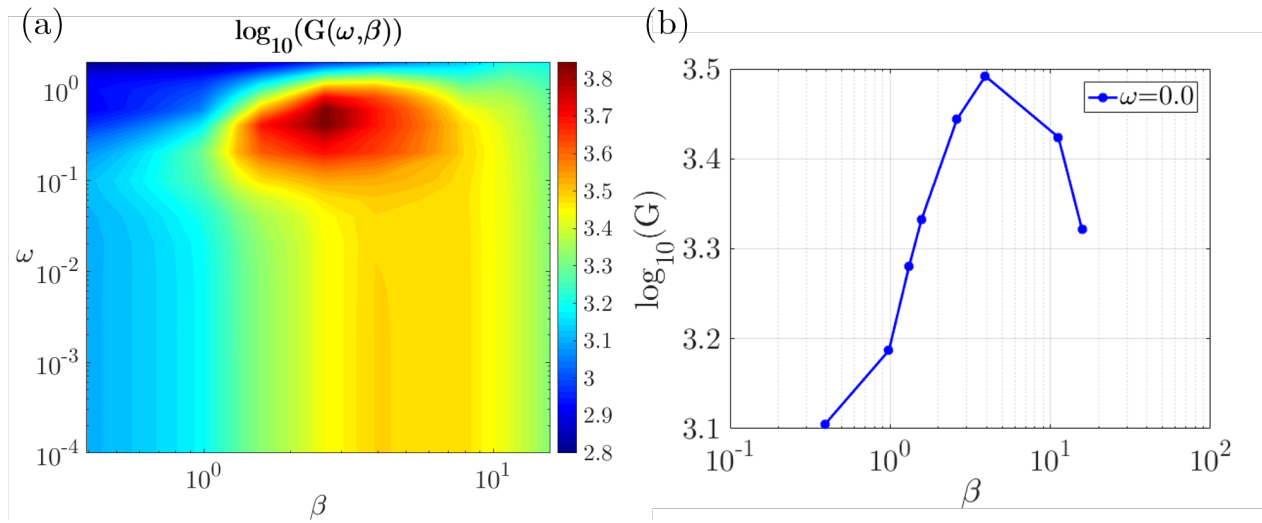


Fig. 8 (a) Optimal amplification as function of circular frequency ω and spanwise wavenumber β plotted on logscale. (b) Optimal amplification at $\omega = 0.0$ as a function of spanwise wavenumber β .

Physically, the optimal input involves high and low momentum zones in the incoming B/L causing the separation bubble to become three dimensional such that the separation line is corrugated. The system responds by producing streamwise streak-like structures which start growing in the recirculation bubble and are amplified further downstream. The response corresponding to maximum amplification is shown in Fig. 11(b).

We conclude that the presence of recirculation zone in SBFI causes significant changes to appear in the frequency response of the flow. Low frequency inputs start to play more dominant role in the overall system dynamics and there is clear selection of spanwise length scale.

3. Role of the recirculation bubble

In the previous section, we observed that the optimal response appears in the form of streamwise vortices. We investigate if this response is solely a result of streamline curvature near reattachment. To answer this question we compute the frequency response of the double wedge flow by not allowing any perturbation development in the recirculation bubble. Numerically, this corresponds to removing the effect of the separation zone on the system response. For convenience we refer to this study as ‘Case 1’ and the one where both the bubble and the boundary layers are involved as ‘Case 2’. We restrict our investigation to steady inputs (i.e. $\omega = 0$).

The optimal input and the corresponding response from this analysis is shown in the Fig. 12. We observe that optimal input consists of streamwise steady perturbation upstream of the streamline curvature, while the optimal response consists of streamwise streaks similar to that observed with the bubble. We compare the optimal amplification in

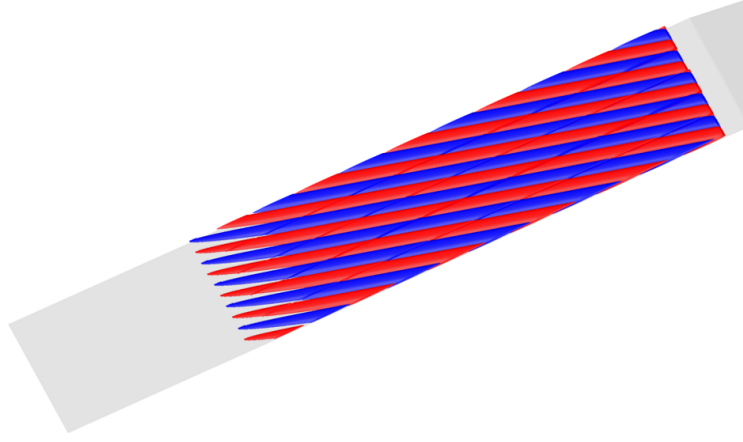


Fig. 9 Isosurface of temperature perturbation response in 12° wedge flow.

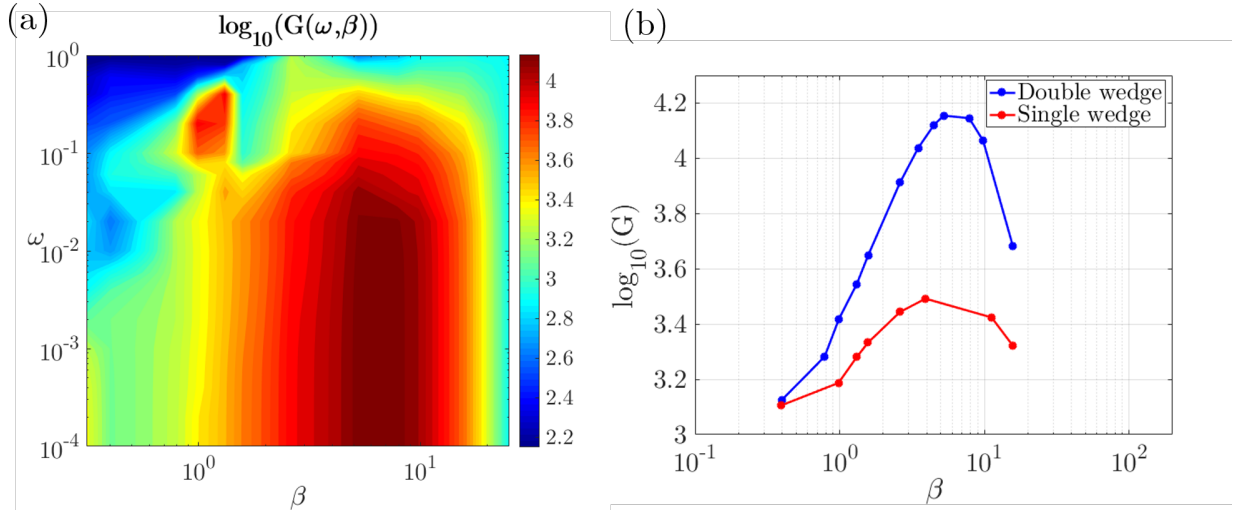


Fig. 10 (a) Optimal amplification as function of circular frequency ω and spanwise wavenumber β plotted on logscale. (b) Optimal amplification at $\omega = 0.0$ as a function of spanwise wavenumber β . Comparison with growth of steady inputs in 12° wedge under identical freestream conditions is shown.

the absence of the bubble to the response of the full system in Fig. 13. In the absence of the bubble, the maximum amplification of the steady perturbations is at least an order of magnitude smaller. Further, a narrower band of spanwise wavelengths are amplified in the absence of the bubble (with $\lambda_{z,max} = 1.1\delta$) compared to that in the presence of the bubble (with $\lambda_{z,max} = 1.8\delta$). However, for inputs with $\lambda_z \rightarrow 0$ the amplification is not affected by the absence of the bubble.

From the results presented in this section, we see that the bubble not only plays a significant role in amplification of the inputs but it is also crucial in selecting a spanwise length scale. Assuming amplification due to only the curved boundary layer over the bubble can lead to significantly different spatio-temporal response than that if it is present.

IV. Conclusions

We consider perturbation growth in high speed boundary layers in the presence of spatially distributed time harmonic three-dimensional perturbation sources (inputs). The linearized Navier-Stokes equations are used for propagation of the perturbations. An input-output analysis is carried out to identify the optimal inputs i.e. inputs to the base flow that result in maximum possible growth of perturbation energy (output). This analysis is repeated for different perturbation frequencies and a frequency response map is computed.

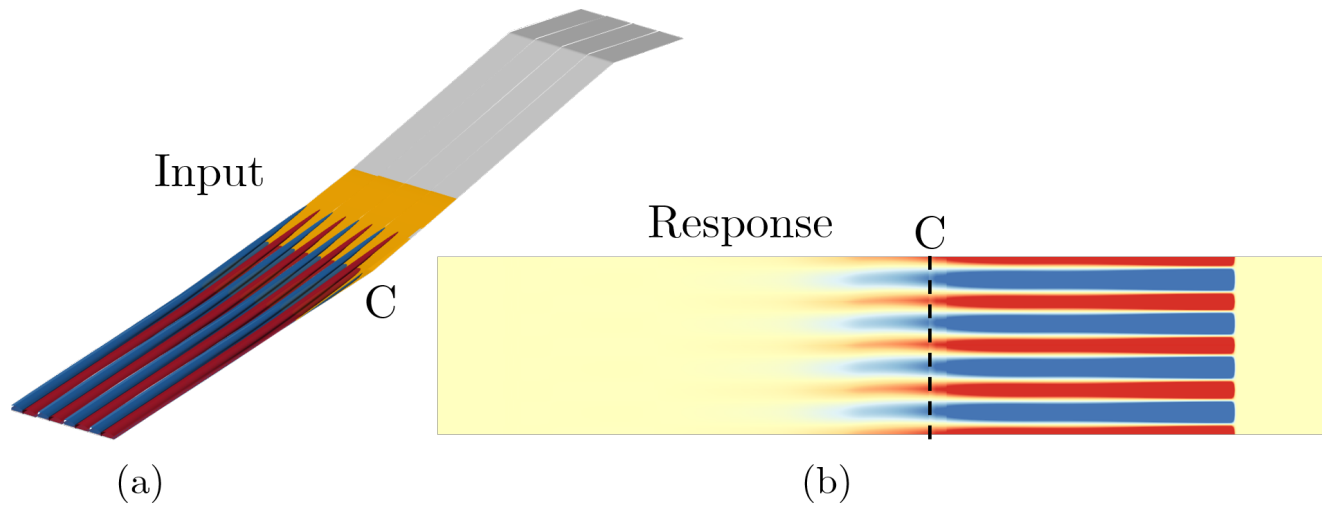


Fig. 11 (a) 3D isosurface of the streamwise vorticity of the input leading to the maximum response. The separation bubble is marked in yellow. (b) Corresponding temperature response at the wall. C denotes the corner of the double wedge in both the cases.

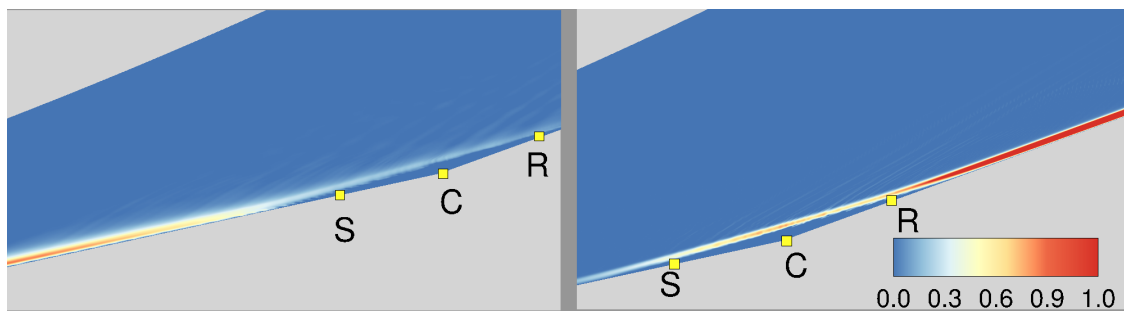


Fig. 12 Optimal steady $(\rho u)'$ input (left) and the corresponding u' response (right) in the absence of the bubble perturbation dynamics.

The state space for the analysis is represented in conserved perturbation variables. A finite volume based discretization for the compressible linear system leads to convenient handling of non-Cartesian grids and geometries. The novel linear system has been validated in previous work by the authors.

We first apply the input-output technique to a Mach 4.5 adiabatic boundary layer over a flat plate with respect to two dimensional perturbations. The analysis demonstrates that the approach can uncover both modal and non-modal perturbation amplification mechanisms without any *a priori* knowledge of the perturbation form. On the flat plate boundary layer, both the Orr mechanism and second mode instability are revealed in the optimal response. The regions where perturbation growth is predicted matches with linear stability theory results reported in literature.

The analysis is then carried out for a complex base state: Mach 5 flow over a slender double wedge. Global stability analysis was carried out on this configuration in our previous work. Here, we analyze a case with turn angle that was found to be globally stable. The flow has several regions where perturbations can grow: a recirculation bubble due to shock boundary layer interaction, a separation-reattachment shock system and highly concave streamline curvature near-reattachment. The frequency response of the flow reveals the selective amplification of low frequency perturbations with a specific wavelength in the spanwise direction. This is contrasted with the frequency response of a single wedge (zero effective turn angle) at the same freestream conditions, where the most amplified perturbations are oblique first modes. We also investigate the role played by the bubble in the optimal perturbation response. The analysis is repeated by excluding perturbation dynamics in the bubble. It is found that the bubble plays a crucial role in perturbation growth and spanwise length scale selection of the ‘Görtler like’ vortices observed in these interactions post-reattachment.

The approach presents itself as the ideal tool to investigate the role of perturbations in the incoming B/L and compare

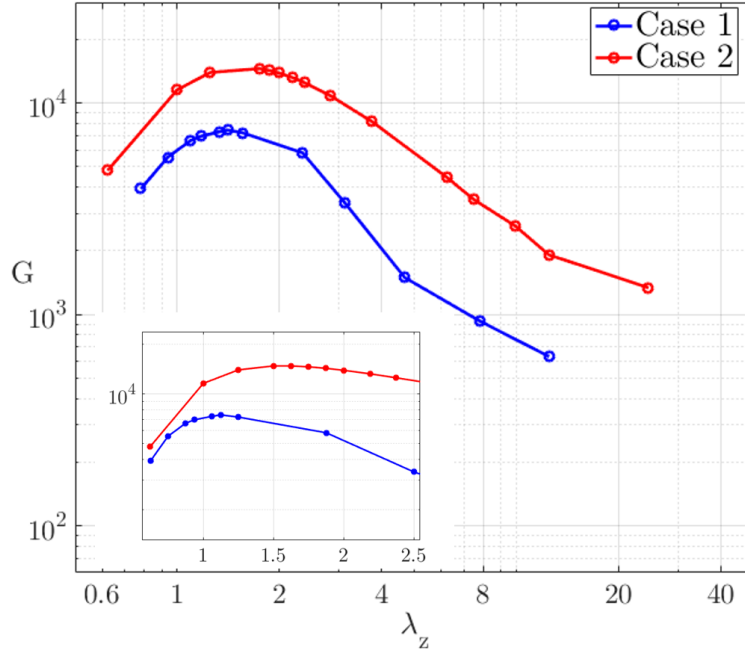


Fig. 13 Optimal growth, $G(\omega = 0)$, as a function of spanwise wavelength λ_z : Case 1: Flow state response without perturbation development in the recirculation bubble and Case 2: Full flow-state response.

it to that of the recirculation bubble in shock-boundary layer interactions. The analysis can also be readily extended to more complex flow fields where the amplification properties of three dimensional flow structures in different parts of the flow-field can be systematically interrogated. Knowledge of critical perturbation growth mechanisms using this approach can help towards predictive transition capabilities in high speed boundary layer flows.

Appendix

A. Viscous flux matrices

In section II, the viscous flux is written in the form $\mathbf{F}_j^v = \mathbf{M}_{jk} \frac{\partial}{\partial x_k} \mathbf{V}$. The viscous flux matrices \mathbf{M}_{ij} have entries that contain the velocity components u_i and transport coefficients μ, λ, κ and can be written in the form

$$\mathbf{M}_{ij} = - \begin{bmatrix} 0 & 0 & 0 & 0 & 0 \\ 0 & a_{11} & a_{12} & a_{13} & 0 \\ 0 & a_{21} & a_{22} & a_{23} & 0 \\ 0 & a_{31} & a_{32} & a_{33} & 0 \\ 0 & b_1 & b_2 & b_3 & \kappa \delta_{ij} \end{bmatrix} \quad (21)$$

where $a_{mn} = \mu(\delta_{ij}\delta_{mn} + \delta_{in}\delta_{jm}) + \lambda\delta_{im}\delta_{jn}$, $b_n = u_m a_{mn}$. The matrix $\overline{\mathbf{M}}_j^{\text{VD}}$ that appears in the linearized viscous flux is

$$\overline{\mathbf{M}}_j^{\text{VD}} = \begin{bmatrix} 0 & 0 & 0 & 0 & 0 \\ 0 & 0 & 0 & 0 & 0 \\ 0 & 0 & 0 & 0 & 0 \\ 0 & 0 & 0 & 0 & 0 \\ 0 & \bar{\sigma}_{1j} & \bar{\sigma}_{2j} & \bar{\sigma}_{3j} & 0 \end{bmatrix} \quad (22)$$

B. Disturbance energy norm

The norm of the perturbation is chosen to account for energy in a compressible flow. For the present case we choose Chu's energy norm [28, 39]. We obtain the following definition of the perturbation energy in the domain Ω ,

$$E = \int_{\Omega} \left(\frac{1}{2} \bar{\rho} u'_i u'_i + \frac{\bar{p}}{2} \left(\frac{\rho'}{\bar{\rho}} \right)^2 + \frac{\bar{E}_{\text{int}}}{2} \left(\frac{T'}{\bar{T}} \right)^2 \right) d\Omega \quad (23)$$

Representing, $\mathbf{V}' = \left(\rho' \quad u'_i \quad T' \right)^T$ as the primitive fluctuation variables. We can use the linear transformation to go to conserved fluctuation variables $\mathbf{V}' = \bar{\mathbf{N}} \mathbf{U}'$. Here the transformation matrix, $\bar{\mathbf{N}}$ is given by,

$$\bar{\mathbf{N}} = \frac{\partial V}{\partial U} \Big|_{\bar{U}} = \begin{bmatrix} 1 & 0 & 0 & 0 & 0 \\ -\frac{\bar{U}}{\bar{\rho}} & \frac{1}{\bar{\rho}} & 0 & 0 & 0 \\ -\frac{\bar{p}}{\bar{\rho}} & 0 & \frac{1}{\bar{\rho}} & 0 & 0 \\ -\frac{\bar{W}}{\bar{\rho}} & 0 & 0 & \frac{1}{\bar{\rho}} & 0 \\ \frac{\bar{U}^2 + \bar{V}^2 + \bar{W}^2}{2C_v \bar{\rho}} - \frac{\bar{T}}{\bar{\rho}} & -\frac{\bar{U}}{C_v \bar{\rho}} & -\frac{\bar{V}}{C_v \bar{\rho}} & -\frac{\bar{W}}{C_v \bar{\rho}} & \frac{1}{C_v \bar{\rho}} \end{bmatrix} \quad (24)$$

Using the definition given in Eq. 23 and the definition of in Eq.24, we obtain the following expression for energy, E using conserved fluctuation quantities,

$$E = \frac{1}{2} \int_{\Omega} \mathbf{U}'^H \mathbf{P} \mathbf{U}' d\Omega \quad (25)$$

Here, $\mathbf{P} = \bar{\mathbf{N}}^H \mathcal{M} \bar{\mathbf{N}}$ and \mathcal{M} is given by

$$\mathcal{M} = \begin{bmatrix} \frac{\bar{p}}{\bar{\rho}^2} & 0 & 0 & 0 & 0 \\ 0 & \bar{\rho} & 0 & 0 & 0 \\ 0 & 0 & \bar{\rho} & 0 & 0 \\ 0 & 0 & 0 & \bar{\rho} & 0 \\ 0 & 0 & 0 & 0 & \frac{\bar{E}_{\text{int}}}{\bar{T}^2} \end{bmatrix} \quad (26)$$

C. Power iteration for optimal input and output vectors

In section II.C, the problem of finding the optimal frequency response is posed as an optimization of a quadratic form subject to equality constraints (see Eq. 15). Solution to this constraint optimization problem can then be rewritten as an unconstrained optimization problem [48] by using the following definition of the Lagrangian,

$$\mathcal{L} = \mathcal{J} - \int_{\Omega} \boldsymbol{\Lambda}^H ((i\omega \mathbf{I} - \mathbf{A})\mathbf{q} - \mathbf{B}\mathbf{d}) d\Omega \quad (27)$$

Here, $\boldsymbol{\Lambda}$ is the Lagrange multiplier and

$$\mathcal{J} = G^2 = \frac{\mathbf{d}^H \mathbf{P} \mathbf{d}}{(\mathbf{C}\mathbf{q})^H \mathbf{P} (\mathbf{C}\mathbf{q})} \quad (28)$$

The solution is then obtained by enforcing the following extremality conditions on \mathcal{L} ,

$$\frac{\delta \mathcal{L}}{\delta \boldsymbol{\Lambda}} = \mathbf{0}, \quad \frac{\delta \mathcal{L}}{\delta \mathbf{q}} = \mathbf{0}, \quad \frac{\delta \mathcal{L}}{\delta \mathbf{d}} = \mathbf{0} \quad (29)$$

The conditions described in Eq. 29 are satisfied and hence the optimization problem (Eq. 15) is solved by using the following iterative algorithm,

- 1) At the k^{th} step assume that \mathbf{d}^k is the optimal input. Compute,

$$(i\omega\mathbf{I} - \mathbf{A})\mathbf{q}^k = \mathbf{B}\mathbf{d}^k \quad (30)$$

- 2) Compute, \mathcal{J}^k and compute,

$$\bar{\epsilon}^k = \frac{\mathcal{J}^k - \mathcal{J}^{k-1}}{\mathcal{J}^k}$$

If $\bar{\epsilon}^k < \epsilon$ with ϵ user specified convergence parameter then, \mathbf{d}^k is the optimal input and $\mathbf{C}\mathbf{q}^k$ is the optimal response and terminate the iterations. Else, go to step 3.

- 3) Compute the adjoint update,

$$(\omega^*\mathbf{I} - \mathbf{A}^\dagger)\mathbf{\Lambda}^k = -\frac{2\mathcal{L}^k}{(\mathbf{C}\mathbf{q}^k)^H\mathbb{P}(\mathbf{C}\mathbf{q}^k)}\mathbf{C}^H\mathbb{P}\mathbf{C}\mathbf{q}^k \quad (31)$$

Here, \mathbf{A}^\dagger is the adjoint of the linear operator, \mathbf{A} .

- 4) Update the value of input using,

$$\mathbf{B}^H\mathbb{P}\mathbf{B}\mathbf{d}^{k+1} = -\frac{(\mathbf{C}\mathbf{q}^k)^H\mathbb{P}(\mathbf{C}\mathbf{q}^k)}{2}\mathbf{B}\mathbf{\Lambda}^k$$

Go to step 1.

The solution to Eq. 30 and Eq. 31 are computed using SuperLU_dist[49].

Acknowledgments

The authors would like to acknowledge the help from Mr. Anthony Knutson in grid construction. This work was sponsored by Air Force Office of Scientific Research under grant number FA9550-12-1-0064 and the Office of Naval Research under grant number N00014-15-1-2522. The views and conclusions contained herein are those of the authors and should not be interpreted as necessarily representing the official policies or endorsements, either expressed or implied, of the funding agencies or the U.S. Government.

References

- [1] Olejniczak, J., Wright, M. J., and Candler, G. V., "Numerical study of inviscid shock interactions on double-wedge geometries," *Journal of Fluid Mechanics*, Vol. 352, 1997, pp. 1–25.
- [2] Ginoux, J., "On Some Properties of Reattaching Laminar and Transitional High Speed Flows,," Tech. rep., Note 53, Von Karman Institute, Rhode-Saint-Genese, Belgium, 1969.
- [3] Simeonides, G., and Haase, W., "Experimental and computational investigations of hypersonic flow about compression ramps," *Journal of Fluid Mechanics*, Vol. 283, 1995, pp. 17–42.
- [4] Roghelia, A., Olivier, H., Egorov, I., and Chuvakhov, P., "Experimental investigation of Görtler vortices in hypersonic ramp flows," *Experiments in Fluids*, Vol. 58, No. 10, 2017, p. 139.
- [5] Zapryagaev, V., Kavun, I., and Lipatov, I., "Supersonic laminar separated flow structure at a ramp for a free-stream mach number of 6," *Progress in Flight Physics*, Vol. 5, EDP Sciences, 2013, pp. 349–362.
- [6] Schrijer, F., "Investigation of Görtler vortices in a hypersonic double compression ramp flow by means of infrared thermography," *Quantitative Infrared Thermography Journal*, Vol. 7, No. 2, 2010, pp. 201–215.
- [7] Ishiguro, Y., Nagai, H., Asai, K., and Nakakita, K., "Visualization of hypersonic compression corner flows using temperature-and pressure-sensitive paints," *Proceedings of the 45th AIAA Aerospace Sciences Meeting and Exhibit, American Institute of Aeronautics and Astronautics*, Reston, VA, 2007, pp. 2007–0118.
- [8] Benay, R., Chanetz, B., Mangin, B., Vandomme, L., and Perraud, J., "Shock wave/transitional boundary-layer interactions in hypersonic flow," *AIAA journal*, Vol. 44, No. 6, 2006, p. 1243.

- [9] Willems, S., Gülhan, A., and Steelant, J., "Experiments on the effect of laminar-turbulent transition on the SWBLI in H₂K at Mach 6," *Experiments in Fluids*, Vol. 56, No. 3, 2015, p. 49.
- [10] Inger, G., "Three-dimensional heat-and mass-transfer effects across high-speed reattaching flows," *AIAA Journal*, Vol. 15, No. 3, 1977, pp. 383–389.
- [11] De Luca, L., Cardone, G., De La Chevalerie, D. A., and Fonteneau, A., "Viscous interaction phenomena in hypersonic wedge flow," *AIAA journal*, Vol. 33, No. 12, 1995, pp. 2293–2298.
- [12] de la Chevalerie, D. A., Fonteneau, A., De Luca, L., and Cardone, G., "Görtler-type vortices in hypersonic flows: the ramp problem," *Experimental thermal and fluid science*, Vol. 15, No. 2, 1997, pp. 69–81.
- [13] Görtler, H., "Dreidimensionale Instabilität der ebenen Staupunktströmung gegenüber wirbelartigen Störungen," *50 Jahre Grenzschichtforschung*, Vol. 304, 1955.
- [14] Hall, P., "The linear development of Görtler vortices in growing boundary layers," *Journal of Fluid Mechanics*, Vol. 130, 1983, pp. 41–58.
- [15] Chuvakhov, P., Borovoy, V. Y., Egorov, I., Radchenko, V., Olivier, H., and Roghelia, A., "Effect of Small Bluntness on Formation of Görtler Vortices in a Supersonic Compression Corner Flow," *Journal of Applied Mechanics and Technical Physics*, Vol. 58, No. 6, 2017, pp. 975–989.
- [16] Yao, Y., Krishnan, L., Sandham, N., and Roberts, G., "The effect of Mach number on unstable disturbances in shock/boundary-layer interactions," *Physics of Fluids*, Vol. 19, No. 5, 2007, p. 054104.
- [17] Navarro-Martinez, S., and Tutty, O., "Numerical simulation of Görtler vortices in hypersonic compression ramps," *Computers & fluids*, Vol. 34, No. 2, 2005, pp. 225–247.
- [18] Robinet, J.-C., "Bifurcations in shock-wave/laminar-boundary-layer interaction: global instability approach," *Journal of Fluid Mechanics*, Vol. 579, 2007, pp. 85–112.
- [19] Hildebrand, N., Dwivedi, A., Nichols, J. W., Jovanović, M. R., and Candler, G. V., "Simulation and stability analysis of oblique shock-wave/boundary-layer interactions at Mach 5.92," *Phys. Rev. Fluids*, Vol. 3, 2018, p. 013906.
- [20] GS, S., Dwivedi, A., Candler, G. V., and Nichols, J. W., "Onset of three dimensionality in supersonic flow over a slender double wedge," *Physical Review Fluids*, Submitted, ????
- [21] Schmid, P. J., "Nonmodal stability theory," *Annu. Rev. Fluid Mech.*, Vol. 39, 2007, pp. 129–162.
- [22] Chomaz, J.-M., "Global instabilities in spatially developing flows: non-normality and nonlinearity," *Annu. Rev. Fluid Mech.*, Vol. 37, 2005, pp. 357–392.
- [23] Trefethen, L. N., "Pseudospectra of linear operators," *SIAM review*, Vol. 39, No. 3, 1997, pp. 383–406.
- [24] JOVANOVIĆ, M. R., and Bamieh, B., "Componentwise energy amplification in channel flows," *Journal of Fluid Mechanics*, Vol. 534, 2005, pp. 145–183.
- [25] Reshotko, E., and Tumin, A., "Role of transient growth in roughness-induced transition," *AIAA journal*, Vol. 42, No. 4, 2004, pp. 766–770.
- [26] Reshotko, E., "Transient growth: a factor in bypass transition," *Physics of Fluids*, Vol. 13, No. 5, 2001, pp. 1067–1075.
- [27] Paredes, P., Choudhari, M. M., and Li, F., "Blunt-body paradox and transient growth on a hypersonic spherical forebody," *Physical Review Fluids*, Vol. 2, No. 5, 2017, p. 053903.
- [28] Hanifi, A., Schmid, P. J., and Henningson, D. S., "Transient growth in compressible boundary layer flow," *Physics of Fluids*, Vol. 8, No. 3, 1996, pp. 826–837.
- [29] Zhong, X., and Wang, X., "Direct numerical simulation on the receptivity, instability, and transition of hypersonic boundary layers," *Annual Review of Fluid Mechanics*, Vol. 44, 2012, pp. 527–561.
- [30] Ma, Y., and Zhong, X., "Receptivity of a supersonic boundary layer over a flat plate. Part 1. Wave structures and interactions," *Journal of Fluid Mechanics*, Vol. 488, 2003, pp. 31–78.
- [31] Malik, M., Lin, R.-S., and Sengupta, R., "Computation of hypersonic boundary-layer response to external disturbances," *37th Aerospace Sciences Meeting and Exhibit*, 1999, p. 411.

- [32] Zhou, K., Doyle, J. C., Glover, K., et al., *Robust and optimal control*, Vol. 40, Prentice hall New Jersey, 1996.
- [33] Skogestad, S., and Postlethwaite, I., *Multivariable feedback control: analysis and design*, Vol. 2, Wiley New York, 2007.
- [34] Jovanović, M. R., “Modeling, analysis, and control of spatially distributed systems,” Ph.D. thesis, University of California, Santa Barbara, 2004.
- [35] Brandt, L., Sipp, D., Pralits, J. O., and Marquet, O., “Effect of base-flow variation in noise amplifiers: the flat-plate boundary layer,” *Journal of Fluid Mechanics*, Vol. 687, 2011, pp. 503–528.
- [36] Jeun, J., Nichols, J. W., and Jovanović, M. R., “Input-output analysis of high-speed axisymmetric isothermal jet noise,” *Physics of Fluids*, Vol. 28, No. 4, 2016, p. 047101.
- [37] Fosas de Pando, M., and Schmid, P. J., “Optimal frequency-response sensitivity of compressible flow over roughness elements,” *Journal of Turbulence*, Vol. 18, No. 4, 2017, pp. 338–351.
- [38] MacCormack, R. W., *Numerical computation of compressible and viscous flow*, American Institute of Aeronautics and Astronautics, 2014.
- [39] Chu, B.-T., “On the energy transfer to small disturbances in fluid flow (Part I),” *Acta Mechanica*, Vol. 1, No. 3, 1965, pp. 215–234.
- [40] Candler, G., Barnhardt, M., Drayna, T., Nompelis, I., Peterson, D., and Subbareddy, P., “Unstructured Grid Approaches for Accurate Aerothermal Simulations,” Tech. rep., AIAA-2007-3959, June, 2007.
- [41] Gs, S., Dwivedi, A., Candler, G. V., and Nichols, J. W., “Global linear stability analysis of high speed flows on compression ramps,” *47th AIAA Fluid Dynamics Conference*, 2017, p. 3455.
- [42] Mack, L. M., “Boundary-layer linear stability theory,” Tech. rep., CALIFORNIA INST OF TECHNOLOGY PASADENA JET PROPULSION LAB, 1984.
- [43] Schmid, P. J., and Henningson, D. S., *Stability and transition in shear flows*, Vol. 142, Springer Science & Business Media, 2012.
- [44] Johnson, H., and Candler, G., “Hypersonic boundary layer stability analysis using PSE-Chem,” *35th AIAA Fluid Dynamics Conference and Exhibit*, 2005, p. 5023.
- [45] Matsumura, S., Schneider, S. P., and Berry, S. A., “Streamwise vortex instability and transition on the Hyper-2000 scramjet forebody,” *Journal of Spacecraft and Rockets*, Vol. 42, No. 1, 2005, pp. 78–89.
- [46] Caljouw, R., “An experimental investigation of a three-dimensional hypersonic flow on a double ramp geometry using stereo-PIV,” Master’s thesis, Delft University of Technology, 2007.
- [47] Yang, L., Zare-Behtash, H., Erdem, E., and Kontis, K., “Investigation of the double ramp in hypersonic flow using luminescent measurement systems,” *Experimental Thermal and Fluid Science*, Vol. 40, 2012, pp. 50–56.
- [48] Gunzburger, M. D., *Perspectives in flow control and optimization*, Vol. 5, Siam, 2003.
- [49] Li, X. S., and Demmel, J. W., “SuperLU_DIST: A scalable distributed-memory sparse direct solver for unsymmetric linear systems,” *ACM Transactions on Mathematical Software (TOMS)*, Vol. 29, No. 2, 2003, pp. 110–140.